Opto-Electronic Advances

CN 51-1781/TN ISSN (Print) 2096-4579 ISSN (Online) 2097-3993

Modelling-guided inverse design strategy for semitransparent perovskite photovoltaics with customized colors

Seok-Beom Seo, Rira Kang, Eun-Joo Lee, So-Yeon Ju, Min Jae Lee, Byunghong Lee* and Sun-Kyung Kim*

Citation: Seo SB, Kang R, Lee EJ, Ju SY, Lee MJ, Lee BH, Kim SK. Modelling-guided inverse design strategy for semitransparent perovskite photovoltaics with customized colors. *Opto-Electron Adv* **9**, 250218 (2026).

https://doi.org/10.29026/oea.2026.250218

Received: 22 August 2025; Accepted: 25 December 2025; Published online: 10 February 2026

OEA | Opto-Electronic Advances

Article

February 2026, Vol. 9, No. 2

Open Access

Modelling-guided inverse design strategy for semitransparent perovskite photovoltaics with customized colors

Seok-Beom Seo[1†], Rira Kang[2†], Eun-Joo Lee[1†], So-Yeon Ju[2], Min Jae Lee[2], Byunghong Lee[2*] and Sun-Kyung Kim[1*]

Abstract: Urban architects increasingly seek solar windows that deliver both energy generation and aesthetic value. However, existing color-engineering strategies rely on absorptive metal layers or lack control over the achievable colors. Here, we present a modelling-guided inverse design strategy that integrates an all-dielectric (ZnS/MgF_2) multilayer into semitransparent perovskite photovoltaics, enabling user-defined colors with minimal spectral loss. Leveraging an active learning algorithm, we mapped the attainable color gamut for ZnS/MgF_2-coated devices with distinct perovskite absorber thicknesses and average visible transmittance (AVT) values. As a representative case, a device with a 110 nm-thick absorber on glass or polyethylene terephthalate (PET), initially exhibiting a reddish-brown tint, was transformed into vivid cyan using a 600 nm-thick all-dielectric multilayer. This tuning retained high AVT—6.5% on glass and 5.3% on PET—while enhancing power conversion efficiency by 20.9% and 10.4%, respectively. Real-world imaging confirmed enhanced aesthetics with see-through visibility, underscoring the practical potential of the inverse-design framework. Moreover, this approach is readily transferable to other thin film photovoltaics, providing a versatile route toward color customizable, transmittance-tunable, and high-efficiency solar windows for buildings, vehicles, and wearable electronics.

Keywords: semitransparent device; building-integrated photovoltaic; color engineering; inverse design; active learning; dielectric coating; interference optics

DOI: 10.29026/oea.2026.250218 | CSTR: 32247.14.oea.2026.250218

Citation: Seo SB, Kang R, Lee EJ et al. Modelling-guided inverse design strategy for semitransparent perovskite photovoltaics with customized colors. *Opto-Electron Adv* **9**, 250218 (2026).

1 Introduction

In densely built urban areas, the deployment of photovoltaic (PV) systems is constrained by a lack of available space[1]. Rooftop- and building-integrated photovoltaics (BIPV) can only provide limited capacity in city centers, and expanding these installations often conflicts with environmental sustainability goals. Clearing forests or other natural land for large PV arrays runs counter to the renewable energy ethos, as it leads to deforestation, habitat loss, and even marine ecosystem disruption when aquatic surfaces are used[2–4]. In light of these challenges, integrating PV functionality into the built environment has become a compelling strategy for scaling up solar energy generation. Burgeoning architectural and automotive trends further amplify the demand for semitransparent PVs that can be seamlessly integrated into transparent surfaces[5]. Modern high-rise buildings and facades feature expansive glass panels, and next-generation electric vehicles (EVs) and autonomous vehicles are incorporating larger panoramic windows.

Accordingly, a variety of semitransparent PV technologies are under exploration, including thin-film $Cu(In,Ga)Se_2$, amorphous silicon, organic, and perovskite (PVSK) PVs[5–15]. Among these options, thin-film PVSK PVs are especially promising because they can be fabricated via low-cost solution processing, their thickness (and hence transparency) is easily tunable, they are amenable to large-area scaling, and they have already demonstrated high power conversion efficiencies (PCEs) both in single-junction and tandem configurations[7,9–11,13]. However, integrating PVSK PVs into windows

Received: 22 August 2025

Accepted: 25 December 2025

Published online: 10 February 2026

[1]Department of Applied Physics, Kyung Hee University, Yongin-si, Gyeonggi-do 17104, Republic of Korea; [2]Energy Devices Research Team, Hyundai Motor Group, Uiwang-si, Gyeonggi-do 16082, Republic of Korea.

†These authors contributed equally to this work.

*Correspondence: BH Lee, E-mail: redboho@hyundai.com; SK Kim, E-mail: sunkim@khu.ac.kr

or other see-through applications poses aesthetic challenges. Semitransparent PVSK films tend to impart a pronounced reddish-brown tint to transmitted light (as illustrated in Fig. 1(a)) due to the strong absorption of their photoactive materials at blue wavelengths. This color cast is often undesirable in architectural and interior settings, where neutral or specific preset colors are preferred for visual comfort.

Therefore, researchers have attempted to address the reddish-brown appearance by incorporating additional spectral-shaping elements into the device stack[6,16–35]. For instance, multilayer coatings incorporating thin (~20 nm) metals have been used to adjust the transmitted spectrum toward a more neutral or custom hue[26]. However, they inevitably introduce nontrivial absorption loss. Consequently, such approaches tend to reduce the overall external quantum efficiency (EQE) and also limit the average visible transmittance (AVT). Other lossy materials-based devices also have AVT limit due to their inevitable absorption[17–19,21,23–24,28,32,34]. Alternatively, patterning the active material into microscale stripes or grids increases transparency by leaving parts of the window clear, but this proportionally reduces photocurrent due to the smaller

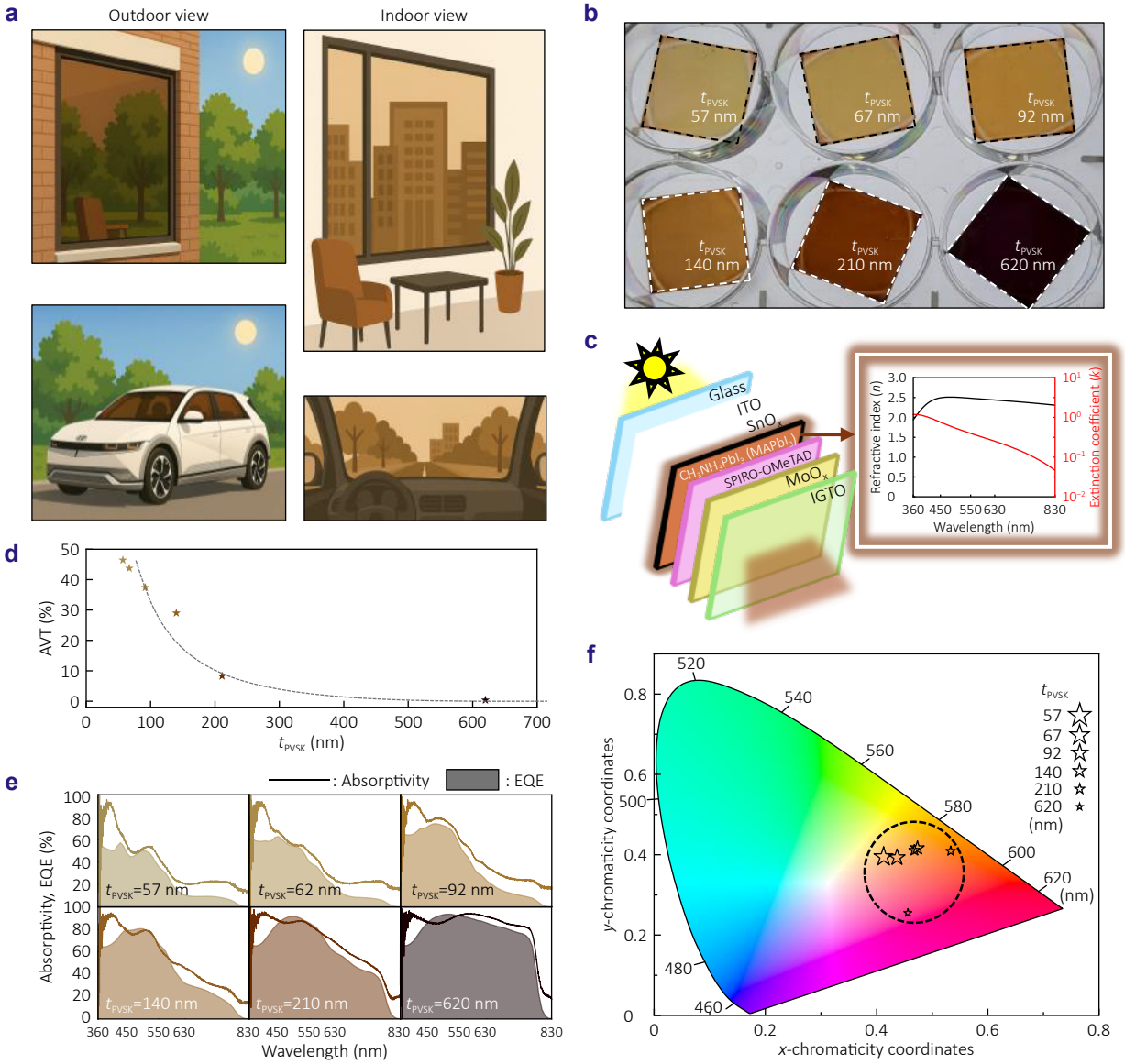

Fig. 1 | Characteristics of semitransparent perovskite (PVSK) photovoltaics (PVs). (a) Applications of semitransparent PVSK PVs in buildings and vehicles. (b) Photographs of semitransparent PVSK PVs with different PVSK thickness (t_{PVSK}), from 57 nm to 620 nm. (c) (Left) Detailed illustration of the PVSK PV stack. (Right) Measured optical constants of $CH_3NH_3PbI_3$ ($MAPbI_3$) PVSK. (d) Relationship between average visible transmittance (AVT) and t_{PVSK}. Colored stars represent measured AVTs of devices in Fig. 1(b). (e) Measured external quantum efficiency (EQE) and absorptivity for various t_{PVSK}. Measurements are conducted with PVs in Fig. 1(b). (f) Transmissive color coordinates of PVs (depicted in Fig. 1(b)) pinned in CIE 1931 chromaticity coordinates.

active area and causes additional fabrication complexity[29,31,33,35].

To address the trade-offs in semitransparent PV design, we developed a modelling-guided inverse design strategy to optimize all-dielectric (ZnS/MgF_2) color-converting multilayer coatings on PVSK devices. These coatings reshape the spectral response to enable user-defined color tuning with minimal spectral loss[20,24,27,34,36–39]. We established an optical model based on measured refractive indices and thicknesses of the full PV device stack, from substrate to top electrodes. To efficiently explore the design space of multilayer coatings, we digitally encoded ZnS/MgF_2 layer sequences as binary strings and trained factorization machines (FMs) to predict the color coordinates of transmitted light through the PV device. This surrogate model was integrated into a quadratic unconstrained binary optimization (QUBO) framework to identify multilayer configurations that best matched desired color and AVT targets[36,39–44]. We applied this inverse-design strategy to exhibit six target colors—red, green, blue, cyan, magenta, and yellow —across PVSK absorber thicknesses ranging from 65 to 165 nm, thereby delineating the achievable color–AVT space. Based on the optimized configurations, we fabricated ZnS/MgF_2 multilayer-coated PVSK PV devices and verified their transmitted spectrum, visual transparency, and power conversion efficiency. We further demonstrated mechanical robustness and flexibility in devices fabricated on PET substrates. Real-world imaging confirmed enhanced visual appeal while preserving see-through transparency, highlighting the potential of our approach for color-customizable solar windows and wearable PVs.

2 Results and discussion

2.1 Optical characteristics of thin-film PVSK PVs

One of the most critical parameters governing the transmittance of semitransparent PVSK PVs is the thickness of the photoactive layer (t_{PVSK}). Devices with t_{PVSK} exceeding 500 nm exhibit an AVT as low as 0.34%, rendering them practically opaque in photographic imaging (Fig. 1(b)). Beyond transparency, the t_{PVSK} also determines the perceived transmitted color. As t_{PVSK} decreases, the transmitted hue gradually shifts from a deep reddish-brown to a yellowish-brown. These transmittances and color characteristics arise mainly from the inherent optical constants of the photoactive material. Specifically, $CH_3NH_3PbI_3$ (Methylammonium lead iodine, $MAPbI_3$) PVSK has a direct bandgap of 1.5 eV (corresponding to 826 nm), and its extinction coefficient increases toward shorter wavelengths (Fig. 1(c))[6,37,45]. Consequently, red light is transmitted more efficiently than shorter-wavelength light, accounting for the characteristic reddish tint. Photons within $MAPbI_3$ absorption band undergo substantial attenuation in accordance with Beer–Lambert law, resulting in an exponential decay of transmission with increasing t_{PVSK} (Fig. 1(d)). Accordingly, reducing t_{PVSK} improves AVT but also diminishes overall photon absorption and EQE (Fig. 1(e)), revealing a fundamental trade-off between transparency and PV performance. In addition, variations in t_{PVSK} subtly modulate the transmitted color. While the hue gradually drifts as a function of thickness, it remains constrained within a reddish-brown region of the color space (Fig. 1(f)), limiting the visual design freedom of uncoated semitransparent PVSK devices. These observations underscore the need for external spectral management to achieve color-customizable, high-performance solar windows.

2.2 Modelling-guided inverse design of all-dielectric coatings

To enable accurate inverse design of all-dielectric coatings (Fig. 2(a)), we initially established a full optical model of the semitransparent PVSK PV device stack. This model incorporated the thicknesses and complex optical constants from the glass/ITO substrate, through the SnO_x electron transport layer and the $MAPbI_3$ photoactive layer, to the $C_{81}H_{68}N_4O_8$ (SPIRO-OMeTAD) hole transport layer and the top MoO_x/IGTO electrode. Spectroscopic ellipsometry provided layer-resolved optical constants (n, k) and physical thicknesses (Fig. S1(a)), while cross-sectional transmission electron microscopy (TEM) confirmed the structural integrity and thicknesses of the multilayer stack (Fig. S2). This whole-device optical model allows the inverse design algorithm to generate dielectric coatings that accurately deliver the desired transmitted color on a real device, thereby minimizing discrepancies between simulated and measured data. To validate this optical model, we chose a reference PVSK device with t_{PVSK} = 110 nm. Feeding the measured optical parameters into a transfer matrix method (TMM) calculation matched a simulated transmittance spectrum that closely matches the measured data of the fabricated PVSK device across the visible range (Fig. 2(b)); the corresponding sRGB colors were nearly identical (Fig. 2(b), inset). This high fidelity provides a reliable foundation for the subsequent inverse optimization of all-dielectric multilayer coatings.

To achieve user-defined transmitted color in semitransparent PVSK devices, we digitally encoded all-dielectric coating positioned on the IGTO anode (Fig. 2(c)). Each coating consisted of 20 elementary layers, each 30 nm thick (t_{bit} = 30 nm, thin enough to remain below the quarter-wave condition across the visible spectrum) resulting in a total stack thickness of 600 nm. Each layer was assigned a binary digit: 0 for low n MgF_2 and 1 for high n ZnS. These two materials can be readily deposited by thermal evaporation and are mechanically stable when alternated in a multilayer. Moreover, due to the near-zero extinction coefficients (k ~ 0) of both materials in the visible spectrum (Fig. S1(b)), the multilayer coating modifies the transmitted colors without

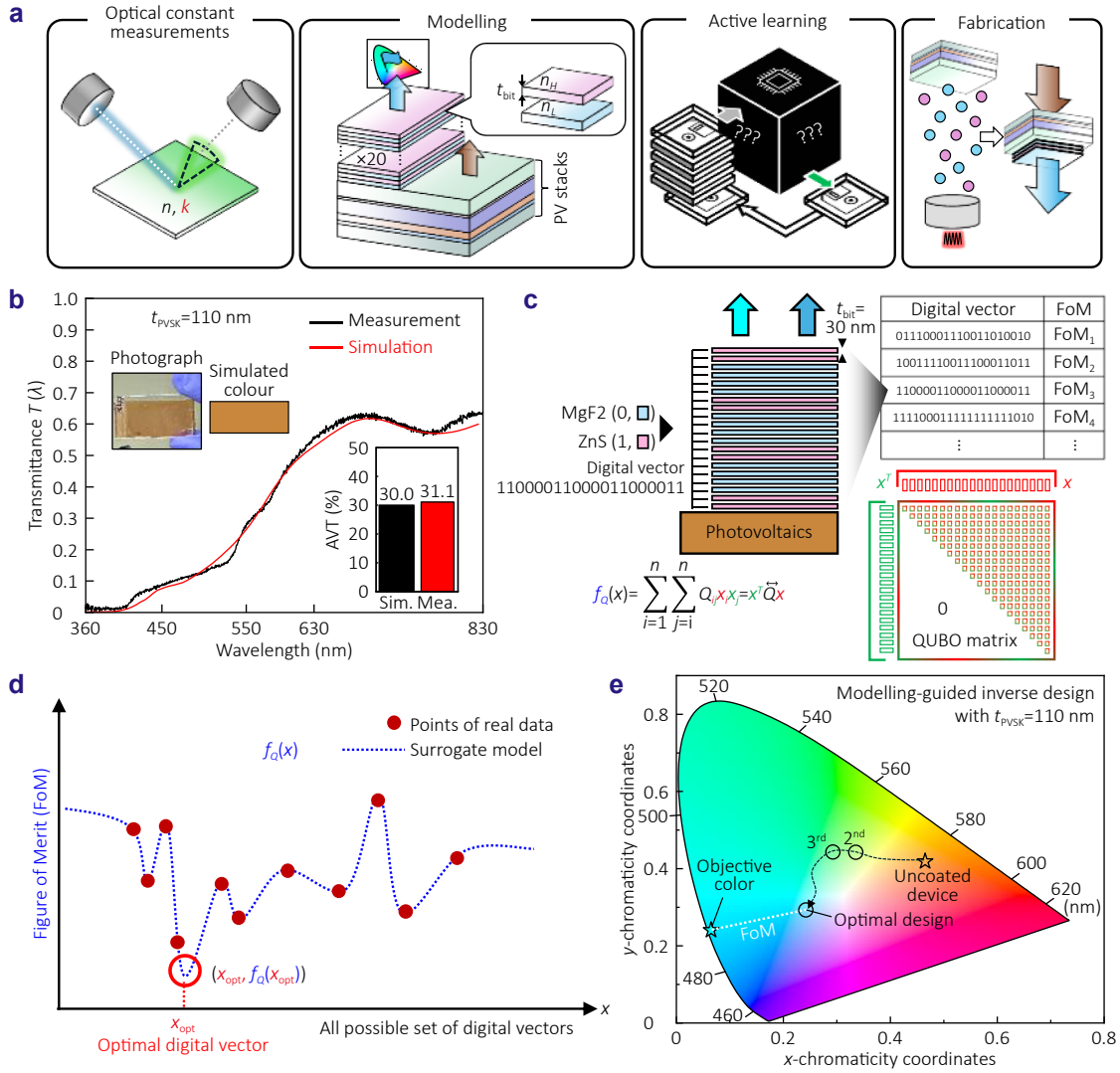

Fig. 2 | Modelling-guided inverse design workflow. (a) Schematic illustration of the workflow. (b) Transmittance spectrum for modelling reliability test between measurement (black) and simulation (red). Inset: Photograph of the PVSK PV of t_{PVSK} = 110 nm which is used for the comparison. (c) Illustration describing binary representation of a 20-layer ZnS/MgF_2 stack (t_{bit} = 30 nm) and QUBO matrix formation. (d) Visualization of surrogate model (blue) and real data (red). (e) Color convergence on the CIE 1931 chromaticity coordinates. During iterations, the color coordinates corresponding to the minimum FoM access toward the objective color (★).

parasitic absorption. Notably, the proposed inverse design approach can also identify optimal multilayers composed of other dielectric pairs (e.g., TiO_2/SiO_2 or Si_3N_4/SiO_2) that achieve comparable performance, provided that they offer a similar refractive index contrast. The 20-bit digital vector spans 2^{20} = 1,048,576 possible sequences. Because exhaustive TMM simulation of all combinations is computationally expensive, we implemented an active learning approach to accelerate convergence. Specifically, we coupled TMM calculations with an FM model trained to predict the color output based on layer sequences. The FM learns the interactions between bits in the digital vector to construct a surrogate model of the figure of merit (FoM), expressed as a quadratic form: $f_Q(x) = \boldsymbol{x}^T \overleftrightarrow{\boldsymbol{Q}} \boldsymbol{x} = \sum_{i=1}^{n} \sum_{j=i}^{n} Q_{ij} x_i x_j$, where $\overleftrightarrow{\boldsymbol{Q}}$ is a symmetric matrix containing both self- and pairwise interaction coefficients between binary variables[36,39–44].

Optimizing this objective function is equivalent to solving a QUBO problem. To identify optimal configurations, we used a brute-force tensor search algorithm that iteratively flipped individual bits in the digital vector to descend the surrogate landscape toward the global minimum (Fig. 2(d)). Initially, 25 sets of digital vectors were generated randomly, while corresponding FoMs were simultaneously evaluated by TMM calculations. The initial dataset comprised 25 randomly generated sequences and their corresponding FoMs evaluated using TMM. Approximately 1,000 active learning cycles were sufficient for convergence. The FoM was defined as the Euclidean distance between the

simulated and target chromaticity coordinates in the CIE 1931 diagram: $FoM = [(x_0-x_{cal})^2+(y_0-y_{cal})^2]^{0.5}$ [46–51]. As the learning cycles progressed, the lowest FoM in the dataset steadily decreased. The resulting transmission spectrum increasingly resembled the target, and the corresponding color coordinates progressively converged toward the desired point in CIE space (Fig. 2(e) and Fig. S3). Optical responses were computed using a transfer-matrix method implemented in MATLAB (custom code).

2.3 Mapping color-transparency of semitransparent PVSK PVs

Tailoring the transmitted color of semitransparent PVSK PVs requires spectral suppression of the wavelengths relevant to the complementary color, inherently reducing the AVT. The transmittance spectra generated during the inverse-design learning cycle shown in Fig. S3 hints at this trade-off; the farther the desired transmitted color deviates from that of the uncoated device, the greater the reduction in transparency. To quantify this relationship, we applied the developed inverse design framework to six primary color targets—red, green, blue, cyan, magenta, and yellow—using three representative photoactive thicknesses (t_{PVSK} = 65, 110, and 165 nm). The baseline AVT values of the uncoated devices were approximately 40%, 30%, and 20%, respectively. For each case, the optimized coating yielded a color output that traced a polygonal boundary in the CIE 1931 diagram, defining the achievable color gamut under constraints of device architecture (Fig. 3(a)). As t_{PVSK} increased, the achievable color gamut narrowed due to greater intrinsic PVSK absorption. Conversely, thinner devices (e.g., the device with t_{PVSK} = 65 nm) began with a native yellowish tint and were tuned to reach a broader chromatic envelope encompassing green and blue hues once the optimized coating was applied. To further examine the interplay between AVT and color tuning, we performed a systematic variation of transparency (from 5% to 20%) for the t_{PVSK} = 110 nm device and mapped the corresponding color gamut (Fig. 3(b)). The results revealed a clear monotonic trend; reducing AVT enabled broader color modulation. This behavior stems from the increasing freedom to suppress or reshape specific spectral bands as transparency constraints are relaxed.

Representative simulated transmission spectra for each primary color illustrate the selective suppression of targeted wavelength regions (Fig. 3(c)). The corresponding perceived colors and resulting AVT values are summarized in Fig. 3(d) and full ZnS/MgF_2 binary sequences for each optimized coating are provided in Fig. S4(a–c). Interestingly, despite variations in t_{PVSK}, coatings optimized for the same target color frequently converged toward similar binary sequences, accounting for the fixed spectral requirements for that color. For example, the cyan coating consistently required suppression of a broad spectral band centered at 630 nm (Fig. S5). Notably, the developed algorithm also identified coating sequences capable of producing a visually neutral gray output (x = 0.33, y = 0.33 in the CIE 1931 diagram). However, beyond a certain photoactive thickness (typically t_{PVSK} > 200 nm), the inherent spectral bias of the uncoated device becomes too pronounced to fully neutralize or redirect toward vivid coloration, even with optimized coatings. Together, these findings delineate the practical design space for balancing color tunability, optical transparency, and PV performance in semitransparent PVSK devices. They also underscore the utility of inverse design as a versatile strategy for navigating the competing demands of aesthetics and functionality in solar windows.

2.4 Characterization of colored semitransparent PVSK PV devices

As discussed earlier, cyan is a particularly stringent test case for the inverse-design framework because it lies far from the native reddish-brown tint of uncoated PVSK devices. To validate the design strategy, we selected a device with t_{PVSK} = 110 nm and deposited 600 nm-thick ZnS/MgF_2 multilayer designed for cyan color conversion. The uncoated reference device appeared deep brown under fluorescent lighting, while the coated device exhibited a vivid cyan appearance, visually confirming the color transformation (Fig. 4(a)). To verify structural fidelity, a glass slide was coated in parallel for cross-sectional scanning electron microscope (SEM) (Fig. 4(b)) and optical spectroscopy (Fig. S6). The measured layer thicknesses deviated from the designed values by less than ±10%, confirming the precision of the fabrication (Fig. S7). Such a deviation range is sufficient to shift the perceived color of the cyan device toward the green or magenta region; to mitigate this, the per-layer thickness error needs to be constrained to approximately ≤ 3 nm (i.e., ≤ 10% of t_{bit} = 30 nm). The measured transmittance spectrum of the coated glass sample showed good agreement with the designed one in both spectral shape and amplitude. However, beyond 630 nm, the fabricated coating exhibited higher transmittance than predicted, resulting in a minor chromatic shift toward magenta.

The measured transmittance spectra of the PVSK devices with and without the color-converting coating corroborate these observations (Fig. 4(c)). The coated device retained a substantial transmittance plateau below 500 nm, crucial for cyan appearance and exhibited an AVT of 6.5%, with peak transmittance reaching 10.4% at 465 nm. For comparison, a previously reported Ag/ITO/Ag anode achieved only ~2% peak transmission and 7.6% of power conversion efficiency (PCE) in analogous blue and green designs. Plotting the measured color coordinates against the designed values in the CIE 1931 diagram confirmed a well-controlled but slightly discernible shift toward the magenta quadrant, consistent with the minor spectral deviation (Fig. 4(d)).

Beyond aesthetics, the multilayer coating also induced a

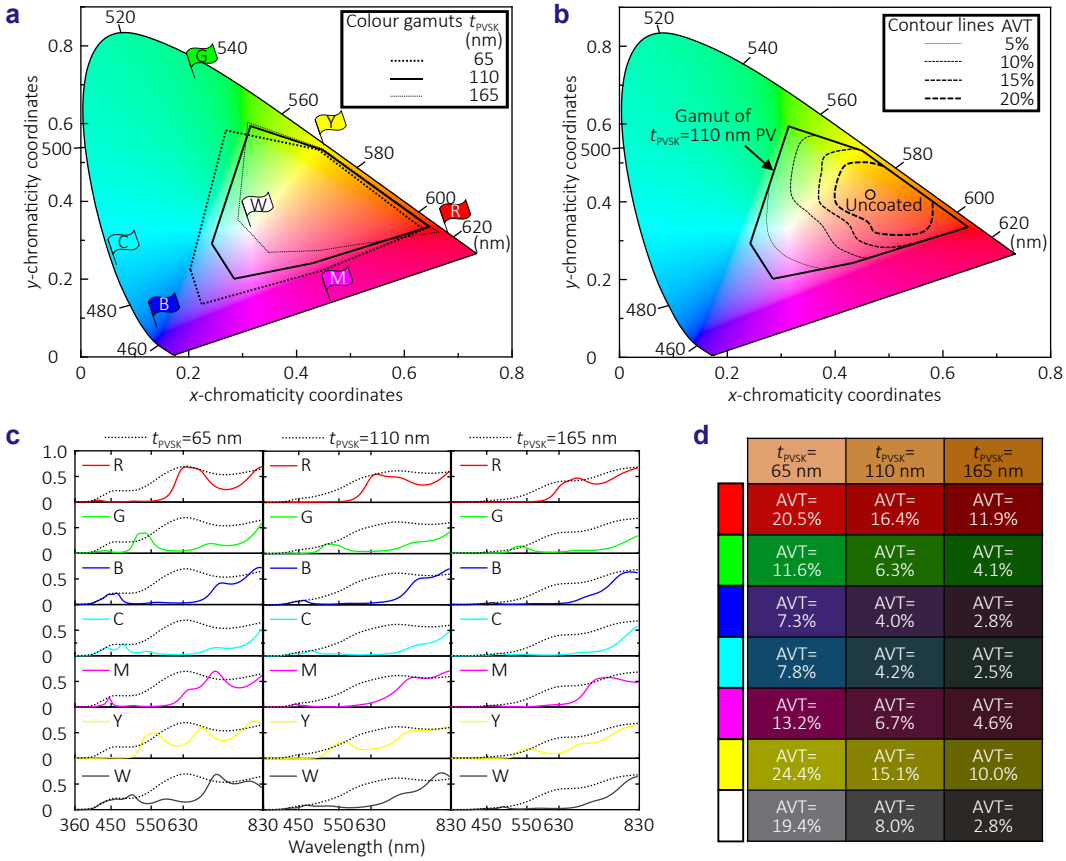

Fig. 3 | Investigation of color gamuts. (a) Color gamut of three PVSK photovoltaics. Markers indicate coordinates of objective six primary colors (R, G, B, C, M, Y) and a neutral (W). Three hexagons are constructed from six vertices, each optimized for one of the six primaries. (b) Trade-off between transmittance and color within the color gamut of t_{PVSK} = 110 nm photovoltaics. (c) Simulated transmittance spectra for six primary and one neutral color target, from left to right at t_{PVSK} = 65, 110, 165 nm. (d) Summary of AVT values and the corresponding transmissive colors shown in (c).

functional enhancement in PV performance. Spectral reshaping within the visible range redirects a portion of incident photons into back-reflected light that is reabsorbed by the PVSK photoactive layer, effectively enhancing sunlight harvesting. Current density–voltage (*J*–*V*) measurements showed an increase in short circuit current density (J_{SC}) from 11.01 to 12.93 mA cm^{-2} (+17.4%) and a corresponding improvement in PCE from 7.64 to 9.24% (+20.9%) (Fig. 4(e)). Given that the device remained unencapsulated during the coating deposition and subsequent handling, further performance gains should be accessible with encapsulation and refined coating deposition. Overall, these results validate the practical feasibility of the modelling-guided inverse-design framework and demonstrate that aesthetic color tuning can coexist with, and even enhance, PV functionality in semitransparent perovskite devices.

2.5 Verification of real-world imaging

The developed modelling-guided inverse-design framework is readily transferable to devices beyond rigid, glass-based PVSK PVs. To demonstrate this versatility, we fabricated a flexible semitransparent PVSK device (t_{PVSK} = 110 nm) on a 100-μm-thick PET substrate (Fig. 5(a)). In this flexible architecture, the transparent IGTO electrode was replaced by an oxide–metal–oxide (OMO) stack composed of ITO/Ag-Pd-Cu alloy (APC)/ITO[49]. The optical constant of each layer in the OMO stack was measured (Fig. S8) and incorporated into the TMM model. Simulated reflectance spectrum based on these parameters closely matched the experimental measurement in Fig. 5(b); the OMO electrode reflected more strongly in the red region while remaining transmissive to blue and green light, which is advantageous for achieving a wide transmitted color gamut (Fig. S9). Due to the metal interlayer in the OMO electrode, the uncoated PET-based device exhibited a lower transparency (AVT = 21.3%) than its glass-based counterpart (Fig. 5(c)). Nonetheless, under the new optical modelling, the inverse design algorithm successfully delivered ZnS/MgF_2 coating sequences, yielding a similarly tuned AVT (see Fig. 4(d) and 5(c)). With this optimized coating, the PET-based device exhibited the intended cyan appearance (Fig. 5(c), inset).

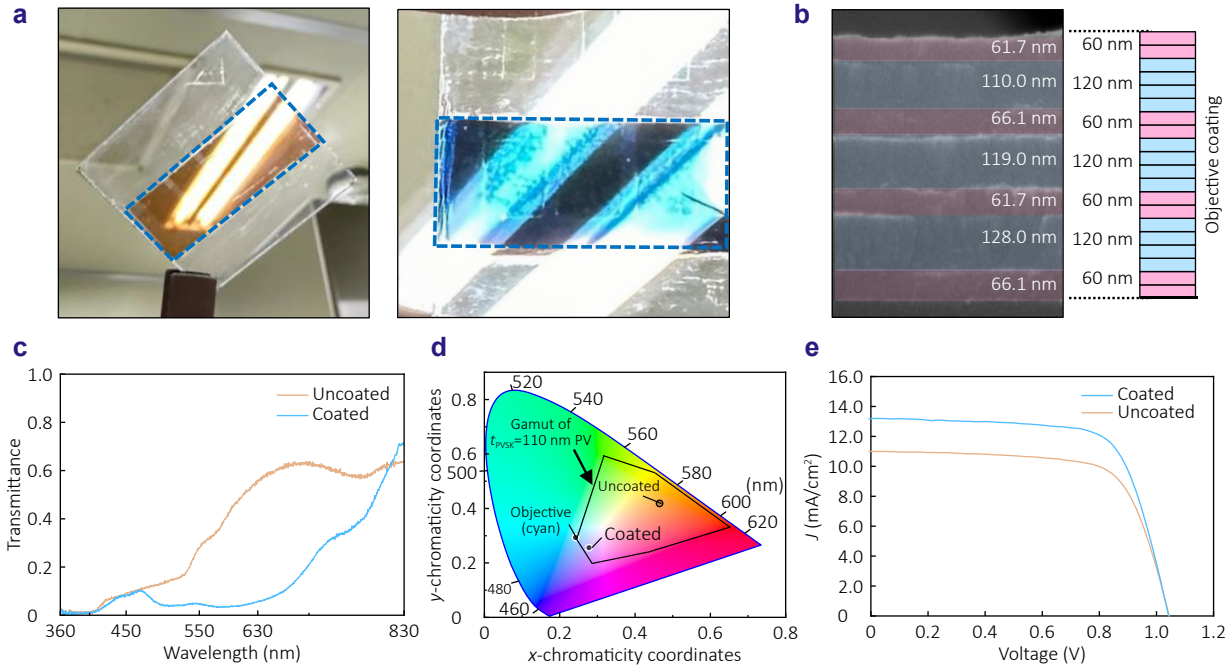

Fig. 4 | ZnS/MgF_2 coated semitransparent PVSK PVs. (a) Photographs of semitransparent PVSK PVs. Left: uncoated, Right: ZnS/MgF_2-coated. (b) SEM image of the ZnS/MgF_2 coating. (c) Optical spectroscopy of uncoated (brown)/coated (blue) semitransparent PVSK PVs. (d) Color coordinates of uncoated/coated semitransparent PVSK PVs in the CIE1931 chromaticity coordinates. (e) Current-voltage (*J*–*V*) curve measurement of uncoated (brown)/coated (blue) semitransparent PVSK PVs.

The corresponding measured transmission spectrum reproduced the simulated target, with an AVT of 5.3% and a peak transmittance of 14.6% at 513 nm (Fig. 5(c)).

While the experimentally derived chromaticity deviated slightly from the target coordinates, the perceptual match was visually compelling. This is attributed to the red-reflective properties of the OMO electrode, which shifted the transmitted spectrum toward the blue–cyan region (Fig. 5(d)). Applying the inverse design framework across the six primary color targets, we mapped the achievable color gamut at t_{PVSK} = 110 nm. Notably, although the PET-based device showed slightly reduced AVT compared to the glass-based device, the color gamut was significantly extended due to spectral shaping of the OMO electrode (Fig. S6). In addition, *J*–*V* measurements showed an increase in *J* from 1.16 to 1.27 mA cm^{-2} (+9.9%) and a corresponding improvement in PCE from 5.24% to 5.78% (+20.9%) (Fig. 5(e)). The PET-based module consisted of multiple cells wired in series and thus operated at higher voltages (~8.0 V) and lower currents than the single junction devices discussed earlier (Fig. 4). Consistent with the photon-recycling pathway in which off-target spectral bands are back-reflected and re-absorbed in the PVSK absorber, Fig. S10 shows that the cyan coating boosts red -band absorptivity with minor changes in the blue where the perovskite already absorbs efficiently. This suggests that the all-dielectric coating delivers a PCE gain that approaches the attainable maximum while keeping the sacrifice in transmittance minimal.

Since all-dielectric coatings function via optical interference, their spectral response is primarily thickness dependent. To examine thickness sensitivity, we progressively varied t_{bit} in the optimized ZnS/MgF_2 sequence from 10 to 50 nm. Deviations of approximately ±10% around t_{bit} = 30 nm covered much of the perceptual hue range including magenta, cyan, and green, while larger deviations eventually saturated both AVT and chromaticity (Fig. 5(f)). Notably, at t_{bit} = 30 nm, AVT reached a minimum, yielding the most pronounced color transformation. Similar trends were observed in the glass-based devices (Fig. S7), confirming the robustness of the design strategy across different platforms.

Finally, outdoor photographs confirmed the visual quality of the fabricated cyan-colored PET-based device. Under direct sunlight, the device appeared as a vivid cyan panel (Fig. 5(g)). When viewed from behind, the skyline was rendered with a cool tint without obstructing details (Fig. 5(h)). Hue shifts near the edges originated from oblique incidence. These effects became more pronounced under bending. Increased curvature enhanced angular dispersion, producing a characteristic rainbow fringe at the periphery (Fig. 5(i)). However, because such bending tests assume extreme curvature, they are unlikely to pose a major issue in typical building-and vehicle-glazing environments. Our analysis of transmitted spectra and color changes over a range of incidence angles supports this assessment (Fig. S11). This behavior further confirms that the observed coloration arises from interference rather than absorption.

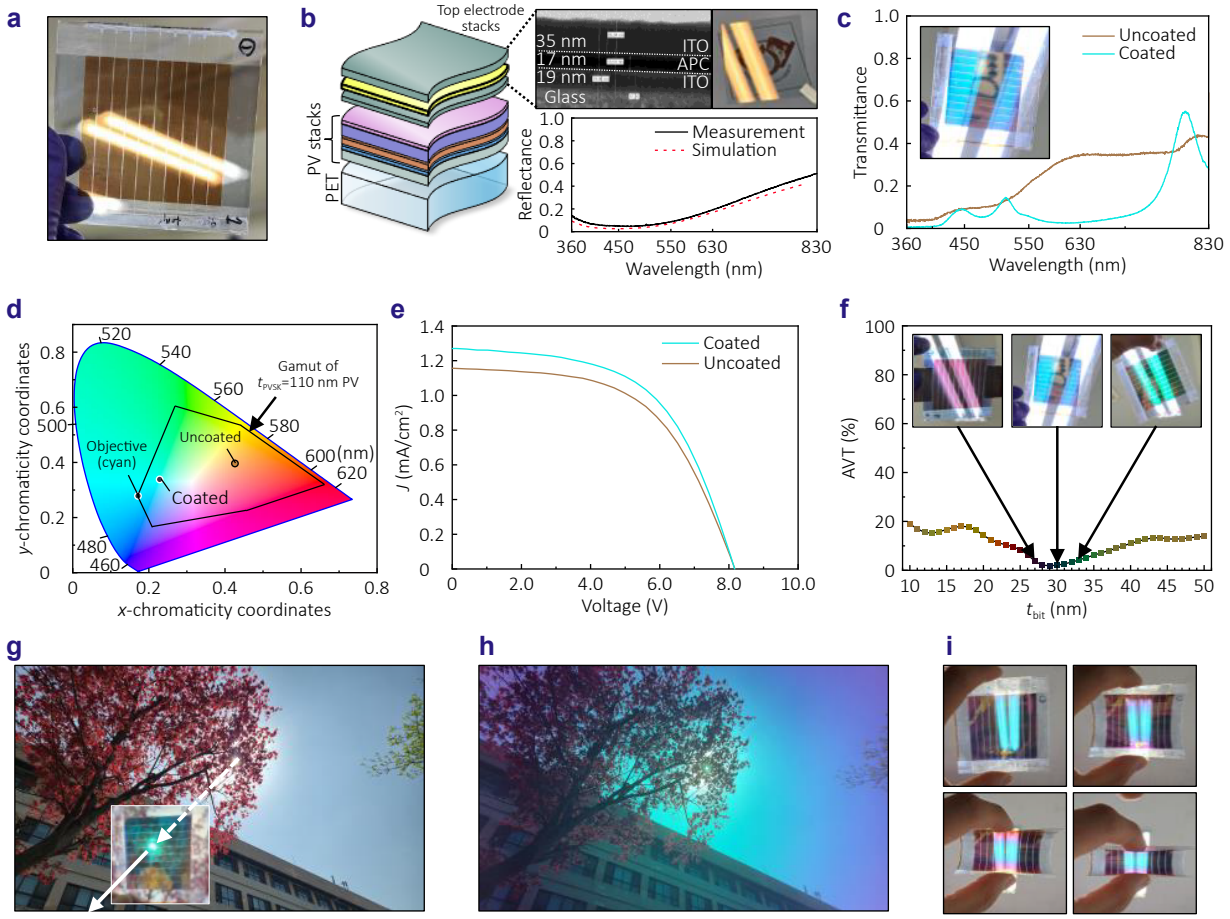

Fig. 5 | Flexible, colored semitransparent PVSK PVs. (a) Photograph of flexible semitransparent PVSK PV module. (b) (left) Detailed illustration of structural information and (upper right) TEM image & photograph of new ITO/Ag-Pd-Cu (APC)/ITO electrode. (lower right) A modelling-reliability test was conducted by comparing measured and simulated reflectance. (c–e), Characterization of uncoated/coated flexible semitransparent PVSK PVs by optical spectroscopy (Fig. 5(c)), CIE 1931 chromaticity coordinates (Fig. 5(d)), and current-voltage curve measurement (Fig. 5(e)). (f) Impact of dielectric thickness (t_{bit}) variation on AVT and colors, based on t_{PVSK} = 110 nm PV module. (g, h) Real-world images of the device without (Fig. 5(g)) and with (Fig. 5(h)) the coating. The inset in Fig. 5(g) is the photograph of the coated device under direct sunlight. (i) Bending test for the ZnS/MgF_2 coated flexible semitransparent PVSK PVs.

More importantly, the total thickness of the PVSK stack (660 nm, excluding the PET) and dielectric coating (600 nm) sum to only 1.26 μm, affording good mechanical flexibility and allowing repeated bending without cracking or delamination.

3 Conclusions

The modelling-guided inverse design framework developed here enables semitransparent PVSK PVs to display vivid, user-defined transmitted colors while maintaining or even enhancing device efficiency. By embedding a TMM optical model into an active learning loop and restricting the coating layers to purely dielectric, non-absorbing materials, we eliminated the need for lossy metallic color filters and overcame the intrinsic reddish-brown hue characteristic of semitransparent $MAPbI_3$ PVSK devices. On glass-based devices employing an IGTO anode, the optimized ZnS/MgF_2 coating produced a cyan appearance with a peak transmittance of 10.4%, an AVT of 6.5%, and a 20.9% gain in PCE. When the same binary sequence was applied to flexible PET-based devices with an ITO/APC/ITO anode, it achieved a peak transmittance of 14.6%, an AVT of 5.3%, and a 10.4% boost in PCE. All coatings were deposited via thermal evaporation directly onto working PV devices, confirming the practical feasibility of integrating color-tunable interference coatings into real-world modules. To mitigate potential damage from thermal or plasma processes and further preserve device integrity, we also examined an alternative lamination strategy using ZnS/MgF_2 multilayers pre-coated on PET films (Fig. S12). This lamination-based approach expands the manufacturing compatibility of our method.

Because our framework relies solely on accurately measured optical constants, it can be readily adapted to other semitransparent thin-film PV technologies, including organic, CIGS, and tandem devices. This generalizability

presents a universal route toward color-tunable, high-efficiency solar windows suitable for architectural and consumer applications. Future work will focus on expanding both the aesthetic range and PV performance. Thinning the PVSK photoactive layer would increase baseline AVT and enlarge the attainable color gamut. Meanwhile, robust encapsulation strategies are essential for improving device stability against photodegradation and moisture ingress, ultimately enabling higher stabilized efficiencies. On the computational side, transitioning from a 20-bit digital representation to finer discretization, such as 50–100 bits via simulated annealing, or several hundred bits via quantum annealing, could enable sharper spectral control, higher color purity, and access to a broader chromaticity space[40–44]. Together, these advances position colored semitransparent PVSK PVs as a versatile and high-performance solution for a range of transparent power applications, including BIPV, vehicle glazing, and adaptive architectural elements. Our inverse design framework could be further advanced by incorporating complementary strategies from recent developments in multilayer thin-film optimization and intelligent metaphotonics[52–54]. In parallel, emerging photovoltaic manufacturing techniques such as electrospray printing[55] offer scalable routes that may enhance the practicality of our approach for window-integrated applications.

4 Methods

Details on active learning, experimental setup, and fabrication methods are provided in the Supplementary information.

References

1. Nagadi KA. Prospects of building integrated photovoltaics (BIPV) in metropolitan centers of developed countries: a techno-economic assessment. *Energy Syst* (2025).
2. Hernandez RR, Hoffacker MK, Field CB. Land-use efficiency of big solar. *Environ Sci Technol* **48**, 1315–1323 (2014).
3. Kim K, Lee J, Chun KW et al. Analyzing heavy rain-induced damage cases and social perception of mountain photovoltaic power stations in South Korea. *Crisis Emergency Manage* **19**, 81–94 (2023).
4. Choi YK. A study on power generation analysis of floating PV system considering environmental impact. *Int J Software Eng Appl* **8**, 75–84 (2014).
5. Xu CY, Chen YF, Zhao ZJ et al. Semi-transparent photovoltaics. *Energy Environ Sci* **18**, 2095–2135 (2025).
6. Bing JM, Caro LG, Talathi HP et al. Perovskite solar cells for building integrated photovoltaics —glazing applications. *Joule* **6**, 1446–1474 (2022).
7. Shi B, Duan LR, Zhao Y et al. Semitransparent perovskite solar cells: from materials and devices to applications. *Adv Mater* **32**, 1806474 (2020).
8. Li YX, Huang XJ, Sheriff HKM Jr et al. Semitransparent organic photovoltaics for building-integrated photovoltaic applications. *Nat Rev Mater* **8**, 186–201 (2023).
9. Carmona CR, Malinkiewicz O, Betancur R et al. High efficiency single-junction semitransparent perovskite solar cells. *Energy Environ Sci* **7**, 2968–2973 (2014).
10. Gaspera ED, Peng Y, Hou QC et al. Ultra-thin high efficiency semitransparent perovskite solar cells. *Nano Energy* **13**, 249–257 (2015).
11. Khan F, Rezgui BD, Khan MT et al. Perovskite-based tandem solar cells: device architecture, stability, and economic perspectives. *Renew Sustain Energy Rev* **165**, 112553 (2022).
12. Jeong HS, Ki T, Lim D et al. Realizing the potential of scalable and stable semitransparent organic solar modules. *Chem Eng J* **503**, 158497 (2025).
13. Shin MJ, Lee A, Cho A et al. Semitransparent and bifacial ultrathin Cu(In, Ga)Se_2 solar cells via a single-stage process and light-management strategy. *Nano Energy* **82**, 105729 (2021).
14. Shafian S. Semitransparent and colorful solar cell for architectural application. *Future Energy Environ Lett* **2**, 13–32 (2025).
15. Sheng C, Shi YY, Li YZ et al. Semi-transparent colored solar cells for agrivoltaics ecosystem applications. *Adv Sustainable Syst* **9**, 2401059 (2025).
16. Chen WJ, Zhang JW, Xu GY et al. A semitransparent inorganic perovskite film for overcoming ultraviolet light instability of organic solar cells and achieving 14.03% efficiency. *Adv Mater* **30**, 1800855 (2018).
17. Li ZR, Chen BC, Yao LG et al. Asymmetric microcavity to enhance light utilization in colorful semitransparent perovskite solar cells. *Sol Energy* **298**, 113677 (2025).
18. Lee KT, Fukuda M, Joglekar S et al. Colored, see-through perovskite solar cells employing an optical cavity. *J Mater Chem C* **3**, 5377–5382 (2015).
19. Wang H, Li J, Dewi HA et al. Colorful perovskite solar cells: progress, strategies, and potentials. *J Phys Chem Lett* **12**, 1321–1329 (2021).
20. Quiroz COR, Bronnbauer C, Levchuk I et al. Coloring semitransparent perovskite solar cells *via* dielectric mirrors. *ACS Nano* **10**, 5104–5112 (2016).
21. Schlisske S, Mathies F, Busko D et al. Design and color flexibility for inkjet-printed perovskite photovoltaics. *ACS Appl Energy Mater* **2**, 764–769 (2019).
22. Jiang YY, Luo BW, Jiang FY et al. Efficient colorful perovskite solar cells using a top polymer electrode simultaneously as spectrally selective antireflection coating. *Nano Lett* **16**, 7829–7835 (2016).
23. Lee KT, Jang JY, Ha NY et al. High-performance colorful semitransparent perovskite solar cells with phase-compensated microcavities. *Nano Res* **11**, 2553–2561 (2018).
24. Li J, Wang H, Chin XY et al. Highly efficient thermally co-evaporated perovskite solar cells and mini-modules. *Joule* **4**, 1035–1053 (2020).
25. Liu TR, Zhao XM, Wang P et al. Highly transparent, scalable, and stable perovskite solar cells with minimal aesthetic compromise. *Adv Energy Mater* **13**, 2200402 (2023).
26. Lu JH, Yu YL, Chuang SR et al. High-performance, semitransparent, easily tunable vivid colorful perovskite photovoltaics featuring Ag/ITO/Ag microcavity structures. *J Phys Chem C* **120**, 4233–4239 (2016).
27. Lee KT, Jang LY, Park SJ et al. Incident-angle-controlled semitransparent colored perovskite solar cells with improved efficiency exploiting a multilayer dielectric mirror. *Nanoscale* **9**, 13983–13989 (2017).
28. Lu JH, Lin YH, Jiang BH et al. Microcavity structure provides high-performance (>8.1%) semitransparent and colorful organic photovoltaics. *Adv Funct Mater* **28**, 1703398 (2018).
29. Eperon GE, Burlakov VM, Goriely A et al. Neutral color semitransparent microstructured perovskite solar cells. *ACS Nano* **8**, 591–598 (2014).
30. Schaible J, Winarto H, Škorjanc V et al. Optimizing aesthetic appearance of perovskite solar cells using color filters. *Sol RRL* **9**, 2400627 (2025).
31. Kwon HC, Kim A, Lee H et al. Parallelized nanopillar perovskites for semitransparent solar cells using an anodized aluminum oxide scaffold. *Adv Energy Mater* **6**, 1601055 (2016).
32. Almeida E, Alexandre M, Santos IM et al. Photonic-enhanced perovskite solar cells: tailoring color and light capture. *ACS Omega* **9**,

42839–42849 (2024).
33. Kessel A, Jasieniak JJ. Semi-opaque perovskite solar cells. *J Phys Chem Lett* **15**, 9894–9904 (2024).
34. Alkhudhari OM, Wang R, Jia ZY et al. Structurally colored semi-transparent perovskite solar cells using one-step deposition of self-ordering microgel particles. *RSC Adv* **14**, 6190–6198 (2024).
35. Lee W, Yoo YJ, Park J et al. Perovskite microcells fabricated using swelling-induced crack propagation for colored solar windows. *Nat Commun* **13**, 1946 (2022).
36. Yu S, Yu JS, Chen ZH et al. Ultrahigh visible-transparency, submicrometer, and polymer-free radiative cooling meta-glass coating for building energy saving. *ACS Photonics* **11**, 3412–3423 (2024).
37. Lee JH, Song Y, Jung K et al. Colored MAPbI3 perovskite solar cells based on SnO_2-SiO_2 distributed Bragg reflectors. *Mater Lett* **282**, 128828 (2021).
38. Yoo GY, Azmi R, Kim C et al. Stable and colorful perovskite solar cells using a nonperiodic SiO_2/TiO_2 multi-nanolayer filter. *ACS Nano* **13**, 10129–10139 (2019).
39. Seo SB, Lee JG, Yu JS et al. Visible transparency modulated cooling windows using pseudorandom dielectric multilayers. *Nanophotonics* **14**, 1587–1595 (2025).
40. Park GT, Kang R, Lee B et al. Binary-optimization-based multilayers and their practical applications. *Curr Opt Photonics* **8**, 545–561 (2024).
41. Park J, Xu ZH, Park GM et al. Inverse binary optimization of convolutional neural network in active learning efficiently designs nanophotonic structures. *Sci Rep* **15**, 15187 (2025).
42. Guo J, Ju SH, Lee Y et al. Photonic design for color compatible radiative cooling accelerated by materials informatics. *Int J Heat Mass Transfer* **195**, 123193 (2022).
43. Kim S, Park SJ, Moon S et al. Quantum annealing-aided design of an ultrathin-metamaterial optical diode. *Nano Converg* **11**, 16 (2024).
44. Kim YB, Park J, Kim JY et al. W-band frequency selective digital metasurface using active learning-based binary optimization. *Nanophotonics* **14**, 1597–1606 (2025).
45. Wang F, Ge CY, Zhou XF et al. Manipulation of crystallization kinetics for perovskite photovoltaics prepared using two-step method. *Crystals* **12**, 815 (2022).
46. Ko G, Noh J, Chae D et al. Neutral-colored transparent radiative cooler by tailoring solar absorption with punctured Bragg reflectors. *Adv Funct Mater* **34**, 2410613 (2024).
47. Lee GJ, Kim YJ, Kim HM et al. Colored, daytime radiative coolers with thin-film resonators for aesthetic purposes. *Adv Opt Mater* **6**, 1800707 (2018).
48. Kim DH, Yoo YJ, Ko JH et al. Standard red green blue (sRGB) color representation with a tailored dual-resonance mode in metal/dielectric stacks. *Opt Mater Express* **9**, 3342–3351 (2019).
49. Ko KJ, Shin SR, Lee HB et al. Fabrication of an oxide/metal/oxide structured electrode integrated with antireflective film to enhance performance in flexible organic light-emitting diodes. *Mater Today Energy* **20**, 100704 (2021).
50. Lee KT, Jang JY, Zhang J et al. Highly efficient colored perovskite solar cells integrated with ultrathin subwavelength plasmonic nanoresonators. *Sci Rep* **7**, 10640 (2017).
51. Zheng JJ, Zhu WD, Xiong JX et al. Multicolored bifacial perovskite solar cells through top electrode engineering. *ACS Appl Mater Interfaces* **17**, 1110–1118 (2025).
52. Ma TG, Wang HZ, Guo LJ. OptoGPT: a foundation model for inverse design in optical multilayer thin film structures. *Opto-Electron Adv* **7**, 240062 (2024).
53. Zhang YN, Chen YG, Wang T et al. Ultrahigh performance passive radiative cooling by hybrid polar dielectric metasurface thermal emitters. *Opto-Electron Adv* **7**, 230194 (2024).
54. Krasikov S, Tranter A, Bogdanov A et al. Intelligent metaphotonics empowered by machine learning. *Opto-Electron Adv* **5**, 210147 (2022).
55. Zhao XY, Deng WW. Printing photovoltaics by electrospray. *Opto-Electron Adv* **3**, 190038 (2020).

Acknowledgements

This work was supported by the Hyundai NGV (R232604.0003), and the National Research Foundation of Korea through the Basic Science Research Program (RS-2023-00207966) and the BK21 FOUR funded by the Ministry of Education and National Research Foundation of Korea (GS-5-JX-NON-20250791 and 2120242015366).

Author contributions

S.-K. Kim and B. Lee supervised the project. S.-B. Seo built active learning framework, fabricated all-dielectric coating on semitransparent perovskite photovoltaics, and conducted optical measurement. E.-J. Lee performed spectroscopic ellipsometry, transmission-electron-microscopy, and energy-dispersive X-ray spectroscopy for all materials composing semitransparent perovskite photovoltaics. R. Kang, M. J. Lee and S.-Y. Ju fabricated semitransparent perovskite photovoltaics and conducted electrical measurements.

Competing interests

The authors declare no competing interests. They have no known competing financial interests or personal relationships that could have appeared to influence the work reported in this paper.

Supplementary information

Supplementary information for this paper is available at
https://doi.org/10.29026/oea.2026.250218